Elasticity of a Pseudoproper Ferroelastic Transition from Stishovite to Post-Stishovite at High Pressure

Yanyao Zhang,[1] Suyu Fu,[1] Baoyun Wang,[1,2] and Jung-Fu Lin[1,*]

[1]*Department of Geological Sciences, Jackson School of Geosciences, The University of Texas at Austin, Austin, Texas 78712, USA*

[2]*State Key Laboratory of Isotope Geochemistry, Guangzhou Institute of Geochemistry, Chinese Academy of Sciences, Guangzhou 510640, China*

(Received 23 July 2020; revised 10 November 2020; accepted 7 December 2020; published 12 January 2021)

Elastic moduli (C_{ij}) of single-crystal stishovite and post-stishovite are determined using Brillouin light scattering, impulsive stimulated light scattering, and x-ray diffraction up to 70 GPa. The C_{12} of stishovite converges with the C_{11} at ~55 GPa, where the transverse wave V_{S1} propagating along [110] also vanishes. Landau modeling of the C_{ij}, B_{1g} optic mode, and lattice parameters reveals a pseudoproper type ferroelastic post-stishovite transition. The transition would cause peculiar anomalies in V_S and Poisson's ratio in silica-bearing subducting slabs in the mid-lower mantle.

DOI: 10.1103/PhysRevLett.126.025701

Introduction.—Ferroelastic transitions are physical phenomena in which crystals undergo a change in point group ("a change of forms") with a symmetry-breaking shear strain [1,2]. Ferroelastic crystals are thus regarded as mechanical analogs of ferromagnetics and ferroelectrics, which are at the heart of novel multiferroic materials for condensed matter physics research and industrial applications [3,4]. Hydrostatic pressure generated in a diamond anvil cell (DAC) can serve as a more effective thermodynamic means than temperature to induce a very large spontaneous strain so the mechanism of the ferroelastic transition could be deciphered [5]. To better understand its underlying driving force, it is of paramount importance to investigate the full sets of elastic moduli (C_{ij}) across the transition [6,7]. Insofar, high-pressure experimental studies on ferroelastic transitions are often limited to optic modes by Raman and infrared spectroscopy as well as lattice parameters and equation of states (EOS) by x-ray diffraction (XRD) [8,9]. Reliable measurements on the full C_{ij}, however, remain limited due to technical challenges in measuring single-crystal sound velocities of both paraelastic and ferroelastic phases across the transition.

Ferroelastic transitions occur naturally in oxides and silicates in Earth's deep crust and mantle, and have been reported to cause seismic velocity anomalies [10,11]. The ferroelastic transition in stishovite (SiO_2) is of particular interest in geophysics due to its abundance of ~25 vol% in basaltic subducting slabs [12]. Stishovite is a prototype of six-fold coordinated oxides and silicates, and is known to display a number of unusual physical properties: a high density of 4.28 g/cm^3, high adiabatic bulk modulus (K_S) of 308 GPa, and high shear modulus (μ) of 228 GPa at ambient conditions [13,14]. Stishovite has also attracted significant interest in materials science as an analog for finding novel superhard and incompressible materials [15]. Previous studies have shown that rutile-type stishovite (space group: $P4_2/mnm$; point group: 422) transforms into $CaCl_2$-type post-stishovite (space group: $Pnnm$; point group: 222) at ~50–55 GPa and room temperature [16]. The tetragonal-to-orthorhombic transition is manifested by a softening of the B_{1g} optic mode in stishovite [17]. In a pseudoproper type Landau model, the order parameter for the transition is bilinearly coupled with a symmetry-breaking shear strain in post-stishovite [18] and the modeled elastic moduli show a significant shear softening across the transition [19–21]. Furthermore, first-principles calculations showed that the transition is driven by a strong coupling between elastic moduli and softening of the B_{1g} mode [22,23]. Direct experimental measurements on single-crystal V_P and V_S to derive full C_{ij} of stishovite and post-stishovite at high pressure would provide key information about the nature of the ferroelastic transition. However, reliable determinations of the full C_{ij} of stishovite are currently limited to ~12 GPa using the Brillouin light scattering (BLS) technique [14,24–26]. This limitation is mainly due to the relatively high V_P of stishovite at ~12–13 km/s that would have overlapped with the V_S of diamond anvils in DACs. Advent on high-pressure velocity measurements of stishovite is also needed to enhance our knowledge of the ferroelastic transition.

In this Letter, we have used both impulsive stimulated light spectroscopy (ISLS) and BLS techniques to measure V_P and V_S of single-crystal stishovite and $CaCl_2$-type post-stishovite up to 70 GPa at room temperature. Together with complementary XRD results, we have solved their full C_{ij} and analyzed acoustic wave dispersions along critical points of the first Brillouin zone across the post-stishovite transition. Based on the pseudoproper type Landau modeling, our results reveal that the transition is driven by the soft

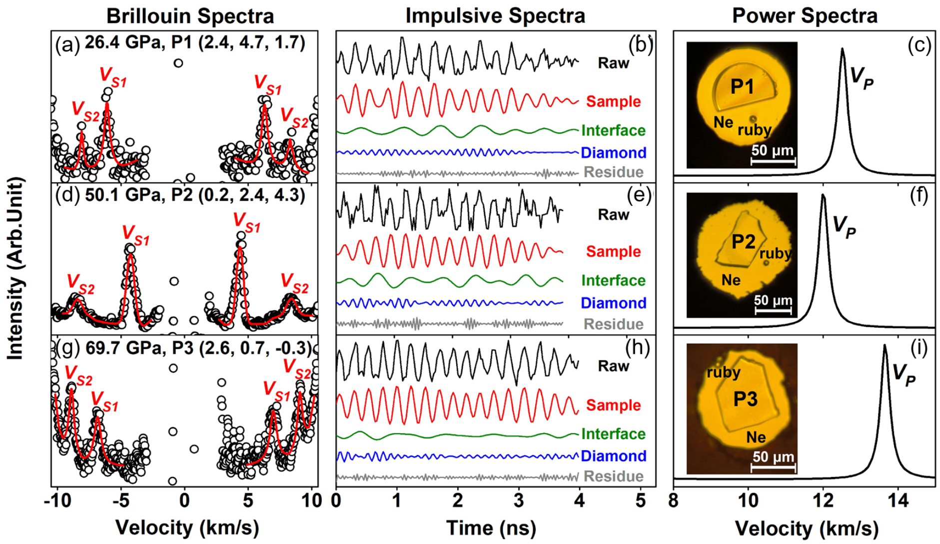

FIG. 1. Representative BLS and ISLS spectra of single-crystal stishovite and post-stishovite at high pressure. Pressures and crystallographic orientations of each platelet are labeled in BLS panels. Open circles in (a), (d), and (g) are collected raw BLS data while red lines are best fits to derive V_{S1} and V_{S2} of the crystal. ISLS spectra in (b), (e), and (h) display signals of the sample, interface, and diamond extracted from the raw data. (c), (f), and (i) are modeled power spectra for the derived V_P of the sample. Insets show representative optical images of the sample chambers.

B_{1g} mode. The coupling between the order parameter and the symmetry-breaking spontaneous strain is manifested by (C_{11}–C_{12}) approaching zero and a disappearance of $V_{S1[110]}$ propagating along [110] and polarizing along [1$\bar{1}$0]. These results of the post-stishovite transition are also used to provide new insights into other ferroelastic transitions as well as abnormal seismic wave signatures in subducting slabs in the lower mantle.

Results.—The collected BLS and ISLS spectra up to 70 GPa display high signal-to-noise ratios and are used to derive V_P and V_S of single-crystal stishovite and post-stishovite at high pressure (Figs. 1 and S1–S5; Tables SI and SII; Text S1 and S2 in the Supplemental Material [27]) [28–34]. Two transverse acoustic velocities with mutually orthogonal polarizations, V_{S1} and V_{S2}, are observed in BLS spectra of both phases, where V_{S2} is larger than V_{S1} by definition. Together with the EOS from XRD results (Figs. S6 and S7; Tables SIII and SIV of the Supplemental Material) [27,35–37], the V_{S1}, V_{S2}, and V_P values as a function of azimuthal angles are used to solve for full C_{ij} of stishovite and post-stishovite at each experimental pressure using Christoffel's equations [38]. Uncertainties of all elastic constants except C_{11} of the post-stishovite phase are sufficiently small for examinations of their pressure-dependent trends across the transition [39] (Text S3 in Ref. [27]). Our derived C_{ij} of stishovite at pressures below 12 GPa are consistent with a previous BLS study (Fig. 2) [14].

The derived C_{ij} of stishovite show that all but C_{11} and C_{12} moduli increase almost linearly with increasing pressure up to 55 GPa (Fig. 2). The three moduli sets of stishovite, principle longitudinal moduli (C_{11} and C_{33}), shear moduli (C_{44} and C_{66}), and off-diagonal moduli (C_{12} and C_{13}), gradually diverge from each other at high pressure. These indicate that the stishovite lattice is

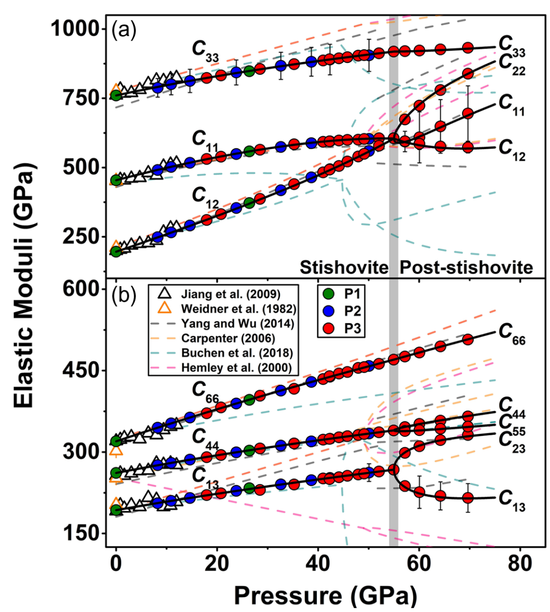

FIG. 2. Elastic moduli of single-crystal stishovite and post-stishovite at high pressure. Solid circles are derived C_{ij} values in this study and solid black lines represent best fits using Landau theory modeling [20,40]. Error bars are smaller than symbols when not shown. The gray vertical band represents the ferroelastic transition region at ~55 GPa. Literature data are also plotted for comparison [14,19,23,24,41,42].

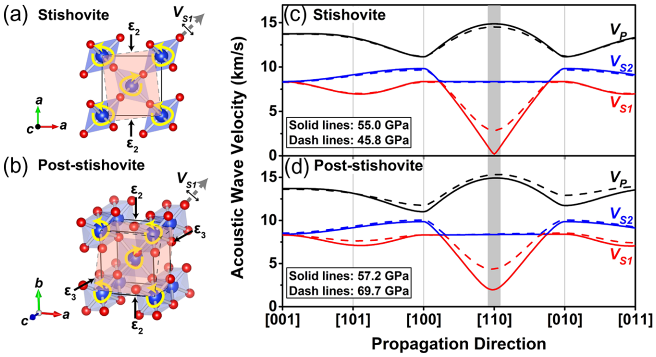

FIG. 3. Lattice distortions and acoustic wave velocity dispersions across the post-stishovite transition at high pressure. (a) and (b) The lattice shear distortion across the ferroelastic transition. Blue and red spheres denote Si and O atoms, respectively. The tetragonal (a) and orthorhombic (b) unit cells under strains are schematically shown in red areas with dashed lines. The strains, labeled as ε_2 and ε_3 depict that the off-diagonal moduli C_{12} and C_{13} become anomalous (see Fig. 2). (c) and (d) Velocity dispersions of V_P (black lines), V_{S2} (blue lines), and V_{S1} (red lines) across the transition. The V_{S1} disappears at the transition that propagates along [110] [dashed gray lines with arrows in (a) and (b)] and has polarization along $[1\bar{1}0]$ (thin black lines with arrows).

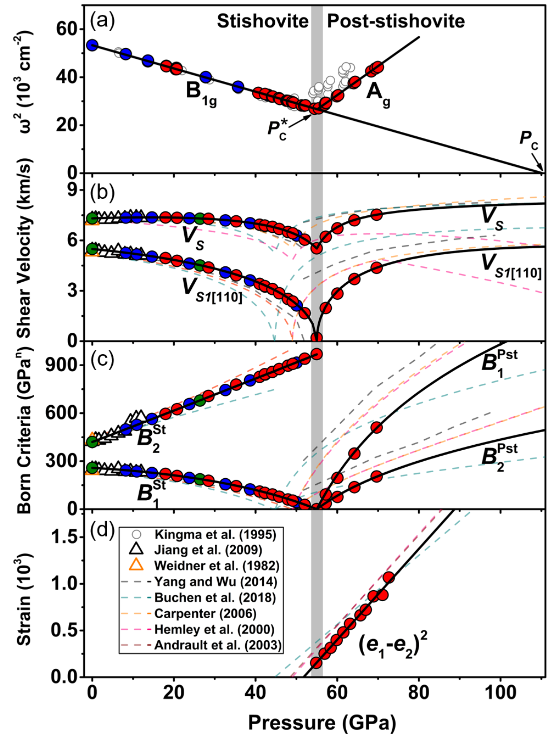

FIG. 4. Optical, elastic, and mechanical behaviors across the post-stishovite transition. (a) Pressure dependence of squared Raman shifts (ω^2) of B_{1g} and A_g mode, where the transition pressure (P_C^*) and critical pressure (P_C) are labeled. (b) $V_{S1[110]}$ vanishes and aggregate V_S softens at the transition. (c) Born stability criteria B_1^{St} (in GPa), B_1^{Pst} (in 5×10^2 GPa^2), and B_2^{Pst} (in 10^6 GPa^3) vanish at the transition whereas B_2^{St} (in 10^3 GPa^2) does not. (d) Squared symmetry-breaking spontaneous strain $(e_1-e_2)^2$ emerges in the post-stishovite phase. Experimental data from this study are plotted as solid circles. Black solid lines are results from the Landau model. Early studies are also shown for comparison [14,17–19,23,24,41,42]. The gray vertical band shows the transition pressure.

experiencing enhanced anisotropic compressional and shear strains with increasing pressure. Most importantly, the C_{12} modulus, which relates a compressional stress (σ) to a perpendicular compressional strain (ε), increases significantly with pressure, while the C_{11} modulus flattens above ~40 GPa. These lead to the convergence of C_{11} and C_{12} at ~55 GPa. That is, the $(C_{11} - C_{12})/2$ constant, which reflects the response of a crystal to deformation caused by shear stress along the [110] direction [47], vanishes at the transition [Fig. 3(a)]. This, in turn, is responsible for the second-order lattice distortion transition where the tetragonal *a* axes of the stishovite phase split into the orthorhombic *a* and *b* axes in the post-stishovite phase [Figs. 3(b) and S7(a) of Ref. [27]]. Such shear-induced lattice distortion also results in rotation of SiO_6 octahedra within the *a* axes plane, causing softening of the B_{1g} optic mode [Figs. 4(a) and S8; Table SV [27]].

Crossing into the orthorhombic post-stishovite, three new elastic moduli C_{22}, C_{55}, and C_{23} emerge and deviate from C_{11}, C_{44}, and C_{13}, respectively, with increasing pressure (Fig. 2). The three principle longitudinal moduli follow the trend $C_{33} > C_{22} > C_{11}$ which indicates anisotropic lattice distortions: the two polar Si─O bonds in the *a*-*b* plane are more compressible than the four equatorial Si─O bonds in the planes parallel to the *c* axis in SiO_6 octahedra, consistent with XRD refinement results [16]. On the other hand, off-diagonal C_{12} and C_{13} moduli, which relate to shear distortions in the [110] and [101] directions, respectively, soften with increasing pressure [Fig. 3(b)]. This leads to an enhanced transverse wave velocity in these directions, and thus, stabilizes the orthorhombic post-stishovite phase [Fig 3(d)].

The elastic moduli results are further used to analyze V_P and V_S dispersions along the principal crystallographic axes ([100], [010], and [001]) and diagonal directions of the principle lattice planes ([101], [011], and [110]) across the post-stishovite transition [Figs. 3(c), 3(d), and 4(b)]. Results show that $V_{S1[110]}$ propagating along [110] and polarizing along $[1\bar{1}0]$ vanishes at ~55 GPa, while all other acoustic waves vary minimally across the transition.

Discussion and implications.—In order to better understand the transformation mechanism, our experimental C_{ij} results as well as Raman and x-ray diffraction data are modeled using the Landau theory with a pseudoproper type energy expansion where the soft B_{1g} mode would lead to the phase transition (Figs. 2, 4, S9, and S10; Table SVI; Text S4 and S5 in the Supplemental Material [27]). This Landau model assumes that the order parameter (Q) is coupled bilinearly with the symmetry-breaking spontaneous strain, $(e_1 - e_2)/\sqrt{2}$ (Eqs. S13 to S15 in Ref. [27]) and the coupling would lead to a nonlinear decrease of the (C_{11}–C_{12}) approaching zero at the transition. The Landau modeling results are very consistent with our experimental elastic moduli across the transition (Fig. 2).

We have also examined the elastic stability across the post-stishovite transition using Born stability criteria [Fig. 4(c)] [48]. Born criteria reflecting the shear stability and the bulk modulus of stishovite are $B_1^{St} = C_{11} - C_{12} > 0$ and $B_2^{St} = C_{33}(C_{11} + C_{12}) - 2C_{13}^2 > 0$, respectively. The ($C_{11}$–$C_{12}$) value in the B_1^{St} criterion is an eigenvalue to a strain eigenvector with the B_{1g} symmetry and the $(e_1 - e_2)/\sqrt{2}$ spontaneous strain based on the group theory [21]. Based on the Landau theory, the consequence of the coupling between the order parameter and the spontaneous strain is that the (C_{11}–C_{12}) value becomes zero at the transition. The B_2^{St}, relating to bulk modulus, remains positive and monotonously increases with pressure. That is, the unit cell volume is subjected to a continuous bulk compression without exhibiting a discontinuous volume collapse in the second-order lattice distortion transition. Furthermore, two Born criteria for the shear stability of the orthorhombic post-stishovite are $B_1^{Pst} = C_{11}C_{22} - C_{12}^2 > 0$ and $B_2^{Pst} = C_{11}C_{22}C_{33} + 2C_{12}C_{13}C_{23} - C_{11}C_{23}^2 - C_{22}C_{13}^2 - C_{33}C_{12}^2 > 0$. These values also become zero at the transition. Finally, the transverse acoustic wave $V_{S1[110]}$ and the two Born stability criteria, B_1^{Pst} and B_2^{Pst}, reemerge at pressures above the transition. The A_g mode in post-stishovite, which has similar vibrational rotations to those of the B_{1g} mode, is also stiffened with increasing pressure.

Putting all the pieces together, our results provide a comprehensive picture for the stishovite to post-stishovite ferroelastic transition. Stishovite undergoes an anisotropic compression under high pressure, which leads to a shear-driven lattice distortion and the softening of the B_{1g} optic mode. The reduction of symmetry, a change of forms from the tetragonal point group to the orthorhombic point group, across the transition induces the symmetry-breaking spontaneous strain in the low-symmetry post-stishovite phase. The soft mode would become imaginary at the critical pressure ($P_C = \sim 110.2$ GPa). However, the transition actually occurs at $P_C^* = \sim 55$ GPa, much lower than the P_C, due to a bilinear coupling between the order parameter and the symmetry-breaking $(e_1 - e_2)/\sqrt{2}$ spontaneous strain [Figs. 4(a) and 4(d)]. This coupling further results in the eigenvalue B_1^{St} (C_{11}–C_{12}) and acoustic wave $V_{S1[110]}$ nonlinearly decreasing to zero with increasing pressure up to P_C^*. Therefore, the post-stishovite transition is clearly driven by the soft B_{1g} mode and belongs to the pseudoproper Landau-type phase transformation [21].

The nature of the post-stishovite transition could be used to understand other ferroelastic systems such as the tetragonal-monoclinic transition in $BiVO_4$ at 1.5 GPa [49]. The optic B_g mode in tetragonal $BiVO_4$ softens close to the transition while the A_g mode in the monoclinic structure stiffens after the transition [50]. The transverse wave V_{S1} in the (001) plane vanishes at the transition in both phases [51]. Our results can thus help elucidate the nature of the ferroelastic transition in other systems.

Our results also have implications on deep-mantle geophysics, where the post-stishovite transition likely occurs at ~1800 km (or 77 GPa and 1706 K) in cold subducting slabs [43]. Using our elasticity data and theoretical predictions to evaluate the high pressure-temperature effect on elasticity [23], the post-stishovite transition would have a minimum aggregate V_S of 5.52 km/s and a Poisson's ratio of 0.363 at ~1800 km depth [44]. Considering a subducting slab containing mid-ocean ridge basalt with ~25 vol% of stishovite [12], the post-stishovite transition would result in approximately 5.4% reduction in V_S and 5.5% enhancement in Poisson's ratio (Text S6 in the Supplemental Material [27]) [45,46]. The effects of the ferroelastic transition on the aforementioned seismic parameters are expected to be distinct from structural transitions and temperature-compositional perturbations more commonly found in the mantle. Seismic observations on the mantle with reduced V_S and enhanced Poisson's ratio near subducting slabs can thus be used as telltale signs [10] to relate to the naturally occurring ferroelastic transition.

Conclusion.—The experimentally derived full C_{ij}, Raman, and x-ray diffraction data of single-crystal stishovite and post-stishovite reveal the nature of the ferroelastic transition at ~55 GPa. Under quasihydrostatic pressure, enhancement of the anisotropic compression leads to the tetragonal-orthorhombic lattice distortion, which is manifested in softening of the B_{1g} optic mode. Because of the coupling of the order parameter with the spontaneous strains, the ferroelastic transition occurs at 55 GPa where the C_{11} modulus converges with the C_{12} modulus and $V_{S1[110]}$ vanishes. As the distortion continues into the orthorhombic post-stishovite phase, large spontaneous strains occur while $V_{S1[110]}$ recovers in the ferroelastic phase. The post-stishovite transition can be well explained by the pseudoproper type energy expansion within the framework of Landau theory. The transition is expected to occur in subducting slabs containing basalt at ~1800 km depth with seismic signatures of ~5.4% V_S reduction and ~5.5% Poisson's ratio enhancement in the lower mantle.

We thank Fang Xu for her assistance in the synthesis and characterization of the single-crystal stishovite crystals. The authors also thank V. Prakapenka and E. Greenberg for their assistance with the synchrotron x-ray diffraction experiments at 13ID-D, GSECARS. GSECARS was supported by the National Science Foundation (EAR-0622171) and U.S. Department of Energy (DE-FG0294ER14466) under Contract No. DE-AC0206CH11357. J.-F. L. acknowledges support from the Geophysics Program of the U.S. National Science Foundation (EAR-1916941) and the Joint-Use User Program of Institute for Planetary Materials, Okayama University.psu.

*Corresponding author.
afu@jsg.utexas.edu

[1] M. V. Klassen-Neklyudova, *Mechanical Twinning of Crystals* (Springer Science & Business Media, New York, 2012).
[2] V. K. Wadhawan, Phase Trans. **3**, 3 (1982).
[3] E. K. Salje, Annu. Rev. Mater. Res. **42**, 265 (2012).
[4] G. Zhang, F. Liu, T. Gu, Y. Zhao, N. Li, W. Yang, and S. Feng, Adv. Electron. Mater. **3**, 1600498 (2017).
[5] M. Guennou, P. Bouvier, G. Garbarino, J. Kreisel, and E. K. Salje, J. Phys. Condens. Matter **23**, 485901 (2011).
[6] E. Gregoryanz and R. J. Hemley, H.-k. Mao, and P. Gillet, Phys. Rev. Lett. **84**, 3117 (2000).
[7] T. Ishidate and S. Sasaki, Phys. Rev. Lett. **62**, 67 (1989).
[8] M. A. Carpenter, E. K. Salje, and A. Graeme-Barber, Eur. J. Mineral. **10**, 621 (1998).
[9] R. L. Moreira, R. P. S. M. Lobo, S. L. L. M. Ramos, M. T. Sebastian, F. M. Matinaga, A. Righi, and A. Dias, Phys. Rev. Mater. **2**, 054406 (2018).
[10] S. Kaneshima, Phys. Earth Planet. Inter. **257**, 105 (2016).
[11] E. K. Salje, Phys. Rep. **215**, 49 (1992).
[12] T. Ishii, H. Kojitani, and M. Akaogi, J. Geophys. Res. **124**, 3491 (2019).
[13] W. Sinclair and A. Ringwood, Nature (London) **272**, 714 (1978).
[14] F. Jiang, G. D. Gwanmesia, T. I. Dyuzheva, and T. S. Duffy, Phys. Earth Planet. Inter. **172**, 235 (2009).
[15] J. Haines, J. Leger, and G. Bocquillon, Annu. Rev. Mater. Res. **31**, 1 (2001).
[16] D. Andrault, G. Fiquet, F. Guyot, and M. Hanfland, Science **282**, 720 (1998).
[17] K. J. Kingma, R. E. Cohen, R. J. Hemley, and H.-k. Mao, Nature (London) **374**, 243 (1995).
[18] D. Andrault, R. J. Angel, J. L. Mosenfelder, and T. L. Bihan, Am. Mineral. **88**, 301 (2003).
[19] R. J. Hemley, J. Shu, M. Carpenter, J. Hu, H.-k. Mao, and K. Kingma, Solid State Commun. **114**, 527 (2000).
[20] M. A. Carpenter, R. J. Hemley, and H.-k. Mao, J. Geophys. Res. **105**, 10807 (2000).
[21] M. A. Carpenter and E. K. Salje, Eur. J. Mineral. **10**, 693 (1998).
[22] B. B. Karki, M. C. Warren, L. Stixrude, G. J. Ackland, and J. Crain, Phys. Rev. B **55**, 3465 (1997).
[23] R. Yang and Z. Wu, Earth Planet. Sci. Lett. **404**, 14 (2014).
[24] D. J. Weidner, J. D. Bass, A. Ringwood, and W. Sinclair, J. Geophys. Res. **87**, 4740 (1982).
[25] A. Yoneda, T. Cooray, and A. Shatskiy, Phys. Earth Planet. Inter. **190**, 80 (2012).
[26] V. Brazhkin, L. McNeil, M. Grimsditch, N. Bendeliani, T. Dyuzheva, and L. Lityagina, J. Phys. Condens. Matter **17**, 1869 (2005).
[27] See Supplemental Material at http://link.aps.org/supplemental/10.1103/PhysRevLett.126.025701 for experimental and modeling details as well as complimentary figures and tables, which includes Refs. [2,14,16,18–26,28–46].
[28] X. Tong, The University of Texas at Austin, 2014, https://repositories.lib.utexas.edu/handle/2152/26108.
[29] J. Yang, X. Tong, J.-F. Lin, T. Okuchi, and N. Tomioka, Sci. Rep. **5**, 17188 (2015).
[30] F. Xu, D. Yamazaki, N. Sakamoto, W. Sun, H. Fei, and H. Yurimoto, Earth Planet. Sci. Lett. **459**, 332 (2017).
[31] S. Fu, J. Yang, N. Tsujino, T. Okuchi, N. Purevjav, and J.-F. Lin, Earth Planet. Sci. Lett. **518**, 116 (2019).
[32] S. Fu, J. Yang, Y. Zhang, T. Okuchi, C. McCammon, H. I. Kim, S. K. Lee, and J.-F. Lin, Geophys. Res. Lett. **45**, 4725 (2018).
[33] A. Dewaele, P. Loubeyre, and M. Mezouar, Phys. Rev. B **70**, 094112 (2004).
[34] Y. Fei, A. Ricolleau, M. Frank, K. Mibe, G. Shen, and V. Prakapenka, Proc. Natl. Acad. Sci. U.S.A. **104**, 9182 (2007).
[35] C. Nisr, K. Leinenweber, V. Prakapenka, C. Prescher, S. Tkachev, and S. H. Dan Shim, J. Geophys. Res. **122**, 6972 (2017).
[36] F. Birch, Phys. Rev. **71**, 809 (1947).
[37] B. Grocholski, S. H. Shim, and V. Prakapenka, J. Geophys. Res. **118**, 4745 (2013).
[38] A. Every, Phys. Rev. B **22**, 1746 (1980).
[39] J.-F. Lin, Z. Mao, J. Yang, and S. Fu, Nature (London) **564**, E18 (2018).
[40] L. Stixrude and C. Lithgow-Bertelloni, Geophys. J. Int. **162**, 610 (2005).
[41] M. A. Carpenter, Am. Mineral. **91**, 229 (2006).
[42] J. Buchen, H. Marquardt, K. Schulze, S. Speziale, T. Boffa Ballaran, N. Nishiyama, and M. Hanfland, J. Geophys. Res. **123**, 7347 (2018).
[43] R. A. Fischer, A. J. Campbell, B. A. Chidester, D. M. Reaman, E. C. Thompson, J. S. Pigott, V. B. Prakapenka, and J. S. Smith, Am. Mineral. **103**, 792 (2018).
[44] R. Hill, Proc. Phys. Soc. London Sect. A **65**, 349 (1952).
[45] J. A. Akins and T. J. Ahrens, Geophys. Res. Lett. **29**, 31 (2002).
[46] A. M. Dziewonski and D. L. Anderson, Phys. Earth Planet. Inter. **25**, 297 (1981).
[47] R. Bell and G. Rupprecht, Phys. Rev. **129**, 90 (1963).
[48] M. Born, *Mathematical Proceedings of the Cambridge Philosophical Society* (Cambridge University Press, Cambridge, England, 1940), p. 160.
[49] R. Hazen and J. Mariathasan, Science **216**, 991 (1982).
[50] D. Errandonea and A. B. Garg, Prog. Mater. Sci. **97**, 123 (2018).
[51] G. Benyuan, M. Copic, and H. Z. Cummins, Phys. Rev. B **24**, 4098 (1981).